Improved LVRT Performance of PV Power Plant Using Recurrent Wavelet Fuzzy Neural Network Control for Weak Grid Conditions

FAA-JENG LIN[ID]**1, (Fellow, IEEE), KUANG-HSIUNG TAN**[ID]**2, WEN-CHOU LUO**[1],
AND GUO-DENG XIAO[1]
[1]Department of Electrical Engineering, National Central University, Chungli 320, Taiwan
[2]Department of Electrical and Electronic Engineering, Chung Cheng Institute of Technology, National Defense University, Taoyuan 335, Taiwan

Corresponding author: Faa-Jeng Lin (linfj@ee.ncu.edu.tw)

ABSTRACT An intelligent control method using recurrent wavelet fuzzy neural network (RWFNN) is proposed to improve the low-voltage ride through (LVRT) performance of a two-stage photovoltaic (PV) power plant under grid faults for the weak grid conditions. The PV power plant comprises an interleaved DC/DC converter and a three-level neutral-point clamped (NPC) smart inverter, in which the output active and reactive powers of the inverter can be predetermined in accordance with grid codes of the utilities. Moreover, for the purpose of improving the control performance of the PV power plant to handle the grid faults for the weak grid conditions, a new RWFNN with online training is proposed to replace the traditional proportional-integral (PI) controller for the active and reactive powers control of the smart inverter. Furthermore, the proposed controllers are implemented by two floating-point digital signal processors (DSPs). From the simulation and experimental results, excellent control performance for the tracking of active and reactive powers under grid faults for the weak grid conditions can be achieved by using the proposed intelligent control method.

INDEX TERMS PV power plant, interleaved DC/DC converter, short-circuit ratio, weak grid, wavelet fuzzy neural network, three-level neutral-point clamped inverter.

I. INTRODUCTION

As the penetration level of inverter-based distributed generators (DGs) including renewable energy resources (RERs) increases, the stability margin of the distribution system may be detrimentally affected. As the DGs are commonly interfaced with the distribution system via power electronic inverters, it is important to take the impact of the control of grid-connected inverter into consideration for the stability analysis of the distribution system integrated with multiple inverter-based DGs. Moreover, the DGs have influences on energy efficiency, voltage profile, reliability and power quality of distribution systems. The size and location of DGs should be carefully selected in order to take advantage of the DGs and limit their negative impacts on system operations [1], [2]. Furthermore, the major challenge for the high penetration of RERs is its intermittent nature, which will lead

The associate editor coordinating the review of this manuscript and approving it for publication was Mu-Yen Chen[ID].

to unanticipated fast power variation rate of the power system thereby pushing the operating points of the power system closer to their stability limits [3]. In addition, reverse power flow caused by the DGs can result in abnormal voltages. When the amount of installed DGs increases, voltage regulation becomes a significant problem, especially in distribution systems where photovoltaic (PV) power plants are widely spread. Additionally, to integrate the DGs with the power networks effectively, the low-voltage ride through (LVRT) requirements have been recently recommended for the installation of large amount of DGs. On the basis of the grid codes, the grid-connected inverters should withstand and remain connected during certain grid faults. Many researches have been proposed in the past decade for the DGs to establish the ability to ride through the grid faults [4]–[7]. To fulfill LVRT requirements under voltage dips, three different control schemes using linear quadratic regulator and symmetrical components have been proposed in [4]. In [5], a two-stage three-phase PV system with three operation mode

was proposed to improve the performance of LVRT and guarantee the power flow balancing between inverter and MPPT during grid faults. In [6], several reference current generation methods, which were developed based on the positive–negative sequence control strategy, were reported to provide the LVRT requirements for the grid-connected inverter based DGs. A Karush–Kuhn–Tucker condition for finding optimal solutions to calculate the inverter's active and reactive current references is proposed in [7]. The proposed methodology takes the X/R ratio at the point of common coupling (PCC) into consideration which allows the inverter to adjust its reference currents to ensure the LVRT [7].

With the increased penetration level of DGs, multiple transformers and long transmission and distribution lines are used to connect the DGs with the public grid owing to the scattered locations of the DGs. Moreover, a public grid with high grid impedance exhibits the characteristics of a weak grid [8]. Recently, short-circuit-ratio (SCR), which can indicate the amount of power that can be accepted by the power system without affecting the power quality at the point of common coupling (PCC), has been used to analyze the strength of the power system at the interconnected points of DGs [9]. In many distribution systems with DGs connected, SCR is less than 10. Furthermore, low SCR values impose serious problems in terms of voltage stability and power quality requirements [10], [11]. Therefore, the development of advanced controller is required to solve the stability problem [11]. In addition, it was found that the voltage instability phenomenon is quite related with the control loops of the inverter such as AC terminal control loop and phase-locked loop (PLL) [12].

It is well known that a combination of neural networks (NNs) and fuzzy logic possesses the advantages of artificial learning in modeling the systems and the benefits of fuzzy reasoning in handling uncertain information. The combined fuzzy neural networks (FNNs) have been demonstrated being effective in different control applications [13], [14]. Moreover, the wavelet transform has been widely used for analyzing the complicated time-varying signals due to its varied window function for the time domain [15], [16]. Recently, the wavelet functions have been proposed to integrate into FNN to construct the wavelet fuzzy neural network (WFNN) for enhancing the adaptive and learning ability in complex engineering issues [17], [18]. Furthermore, owing to the specific structure of a recurrent network with the internal feedback loop to capture system dynamics, the recurrent fuzzy neural network (RFNN) has better dynamic ability than the feed-forward form [19]–[21]. In addition, some researches have combined the recurrent structure with WFNN, i.e., the recurrent wavelet fuzzy neural network (RWFNN), and also has been successfully represented its applicability in various fields [22], [23]. A new RWFNN with online training will be developed in this study.

Since current grid-connected PV power plant lacking the capability of stabilizing output voltage and power under grid faults for the weak grid conditions, an intelligent control method using RWFNN is proposed to improve the LVRT performance of a PV power plant in this study. The operating principles of the PV power plant and the smart inverter will be described in Section II. The characteristics of LVRT for the weak grid conditions will be discussed in Section III. The network structure and online learning algorithms of the proposed RWFNN will be described in Section IV. Moreover, the simulation and experimental results of the intelligent controlled PV power plant using RWFNN will be presented in Sections V and VI. Finally, the conclusions can be found in Section VII.

II. PV POWER PLANT

A 2 kW 3-phase 220 Vrms PV power plant with two-stage circuit architecture is developed in this study as shown in Fig. 1. An interleaved DC/DC converter is considered as the first stage and is responsible to transfer the power energy from the PV panel terminal to the DC bus. The second stage is a three-level neutral-point clamped (NPC) smart inverter and is responsible to dispatch the power from the DC bus to the three-phase grid system. In Fig. 1(a), V_{dc}^* and V_{dc} are the DC bus voltage command and DC bus voltage; $V_{cona,b,c}^*$ is the pulse width modulation (PWM) signal; V_{d1} and V_{d2} are the half high voltage and half low voltage of the DC bus voltage; i_{ao}, i_{bo} and i_{co} are the three-phase currents of the DC/AC inverter; θ_i is the synchronous angle obtained from the double second-order generalized integrator (DSOGI) phase-lock loop (PLL); V_a^*, V_b^* and V_c^* are the three-phase voltage commands of the DC/AC inverter for the sinusoidal PWM (SPWM); V_d^*, V_q^* and V_0^* are the $dq0$-axis SPWM voltage commands of the DC/AC inverter; i_{do}^*, i_{qo}^*, i_{0o}^* and i_{do}, i_{qo}, i_{0o} are the $dq0$-axis current commands and $dq0$-axis currents of the DC/AC inverter. Moreover, in Fig. 1(b), V_{pcc_a}, V_{pcc_b} and V_{pcc_c} are the three-phase voltages of the PCC; $V_{pcc\_a}^+$, $V_{pcc\_b}^+$ and $V_{pcc\_c}^+$ are the positive sequence of three-phase voltages of the PCC; V_{ag}, V_{bg} and V_{cg} are the three-phase voltages of the grid; P^* and Q^* are the active and reactive power commands from LVRT requirements; P and Q are the active and reactive powers; Z_{grid} is the grid impedance of a weak grid.

For the interleaved DC-DC converter, average current control method is adopted where the difference of the DC bus voltage command V_{dc}^* and DC bus voltage V_{dc} is regulated by a proportional-integral (PI) to obtain the current command i_{bat}^* of the DC/DC converter. Then, the current command i_{bat}^* is divided by three for the three arms of the DC/DC converter, and the differences between the current commands and the sensed phase currents i_{bata}, i_{batb}, i_{batc} are regulated via individual PI controller to generate the control signal commands V_{cona}^*, V_{conb}^*, V_{conc}^* for the PWM. For the three-level NPC smart inverter, it is controlled by the $dq0$-axis current control. The d-axis current control is responsible for the reactive power control by using the reactive power current command i_{do}^*. The q-axis current control is responsible for the active power control by using the active power current command i_{qo}^*. First, P^* and Q^* are determined according to the LVRT requirements of the utilities. Then the control
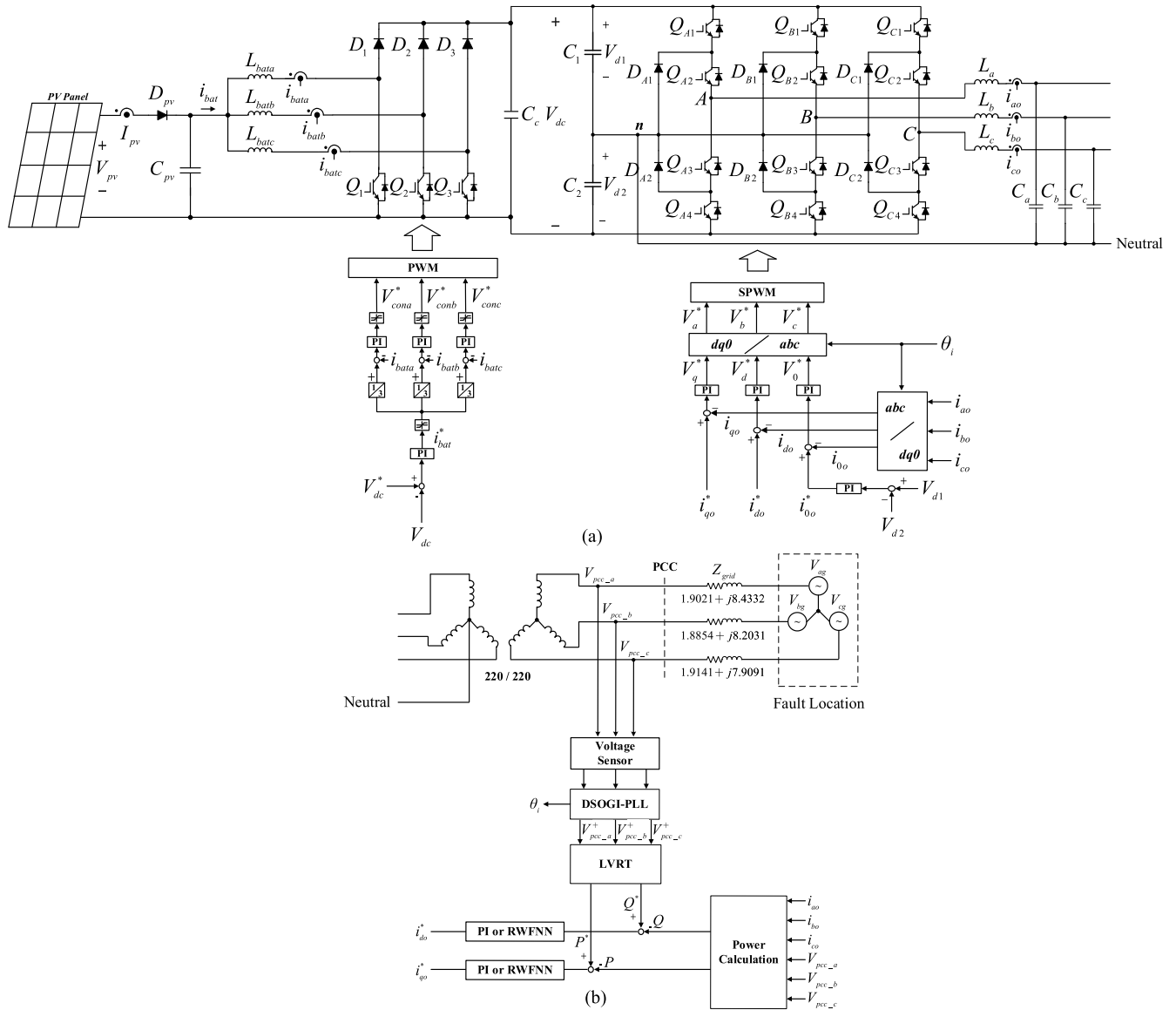
FIGURE 1. Block diagrams of PV system. (a) Interleaved DC/DC converter and three-level NPC inverter, (b) Power calculation for LVRT and weak grid connected.

loop of P regulates the control output i_{qo}^*, which is the active current command, through a PI or the proposed RWFNN controller; the control loop of Q regulates the control output i_{do}^*, which is the reactive current command, also through a PI or the proposed RWFNN controller. Moreover, the 0-axis current control is responsible for the balance of the upper half DC bus voltage V_{d1} and the lower half DC bus voltage V_{d2} by using a PI controller to generate the 0-axis current command i_{0o}^*.

III. CHARACTERISTICS OF LVRT FOR WEAK GRID CONDITIONS

Most grid codes require that the DGs connected to the medium- or high-voltage networks should have the LVRT capability under grid faults. Nowadays, many LVRT standards exist and generally vary across jurisdictions. These requirements are also applied to low-voltage grid owing to the high penetration of the PV power plant in low-voltage grid [24]. Besides keeping connected, some grid codes also prescribe that the DGs should support the grid by supplying reactive power during a grid fault to support and restore the voltage of grid. For instance, the German E.ON LVRT requirements [25] require the DGs to support voltage with additional reactive current during voltage dip where the voltage control must take place within 20 ms (one cycle in Europe) after fault occurrence by providing additional reactive current. The amount of the additional reactive current is 2 % of the rated current for each percent of the voltage dip [25]. Moreover, the maximum amount of the additional reactive current can reach 100 % of rated current if the depth of the voltage dip is greater than 50 %. Therefore, the required percentage of compensation reactive current I_r^* is a function

of the voltage dip V_{dip} can be expressed as:

$$I_r^* = \begin{cases} 0\%, & V_{dip} \leq 0.1 \\ 200V_{dip}\%, & 0.1 < V_{dip} \leq 0.5 \\ 100\%, & V_{dip} > 0.5 \end{cases} \quad (1)$$

Under the condition of unbalance three-phase voltage, the positive sequence of three-phase voltage at the PCC can be calculated as follows:

$$\begin{bmatrix} V_{pcc\_a}^+ \\ V_{pcc\_b}^+ \\ V_{pcc\_c}^+ \end{bmatrix} = \frac{1}{3} \begin{bmatrix} 1 & a & a^2 \\ a^2 & 1 & a \\ a & a^2 & 1 \end{bmatrix} \begin{bmatrix} V_{pcc\_a} \\ V_{pcc\_b} \\ V_{pcc\_c} \end{bmatrix}$$

$$= \sqrt{2} \left| V_p^+ \right| \begin{bmatrix} \sin \theta_i \\ \sin(\theta_i - 2\pi/3) \\ \sin(\theta_i + 2\pi/3) \end{bmatrix} \quad (2)$$

where $a = e^{j2\pi/3}$; $\left| V_p^+ \right|$ is the rms value of the positive sequence of three-phase voltage at the PCC as follows:

$$\left| V_p^+ \right| = \sqrt{\frac{1}{3} \left(V_{pcc\_a}^{+2} + V_{pcc\_b}^{+2} + V_{pcc\_c}^{+2} \right)} \quad (3)$$

In accordance with the LVRT requirements, the amount of the required percentages of the rated current of the compensation reactive current I_r^* during a grid fault depends on the ratio of the voltage reduction at the PCC during the voltage dip. Since there is no LVRT requirement to specify the voltage reduction ratio clearly under the condition of unbalance three-phase voltage, a formula is proposed to evaluate the voltage dip V_{dip} at the PCC as follows [26]:

$$V_{dip} = 1 - \frac{\left| V_p^+ \right|}{V_{base}} pu \quad (4)$$

where V_{base} is the base value of the nominal phase voltage, which equals 127 V in this study. The maximum apparent power can be expressed using the rms value of the upper current limit I_{max} multiplying by the rms values of the three-phase voltages during a grid fault as:

$$|S| = \left(\left| V_{pcc\_a} \right|_{rms} + \left| V_{pcc\_b} \right|_{rms} + \left| V_{pcc\_c} \right|_{rms} \right) I_{max} \quad (5)$$

Thus, the reactive power reference value Q^* and active power reference value P^* can be depicted as follows:

$$Q^* = |S| I_r^* \quad (6)$$
$$P^* = |S| \sqrt{1 - I_r^*} \quad (7)$$

The SCR is defined as follows [12]:

$$SCR = \frac{S_{ac}}{S_N} = \frac{V_g^2}{Z_{grid} S_N} \quad (8)$$

where S_{ac} is the short-circuit capacity of the AC system; S_N is the rated power of the PV power generation; V_g is the line voltage of the grid. Generally, a weak grid in the HVDC system is defined as having SCR < 3 in the IEEE standard 1204-1997. In the standard for distributed energy resources with public grid systems, the grid-connected inverter is required to be operated stably under SCR > 20; a similar

standard in China follows SCR > 10 [8]. However, in many distribution network connected DGs, SCR is less than 10. For a case in Taiwan power company with overhead line 3A477XPW (N-1A300), the Z_{grid} is 0.1249+j0.3142Ω/km; S_N is 6 MW; V_g is 11.4 kV. The SCR is calculated in the following for a 21.35 km overhead line connecting between the PCC and the grid.

$$SCR = \frac{V_g^2}{S_N \times Z_{grid}}$$

$$= \frac{11.4kV \times 11.4kV}{6MW \times (|0.1249 + j0.3142| \times 21.35km)\Omega}$$

$$= \frac{11.4kV \times 11.4kV}{6MW \times 7.219\Omega} = 3 \quad (9)$$

To emulate the above case using the developed PV power plant by simulation, the simulated Z_{grid} should be 1.9565+ j7.8258 Ω to result in the same SCR, which is verified as follows:

$$SCR = \frac{V_g^2}{S_N \times Z_{grid}} = \frac{220 \times 220}{2kW \times (|1.9565 + j7.8258|)\Omega} = 3 \quad (10)$$

Such low SCR value impose serious problems in terms of power stability and quality requirements [10]. In addition, to match the LVRT requirements, the abrupt step commands of active and reactive power will cause oscillation even instability in the output active and reactive powers of the smart inverter owing to the moving of system eigenvalues to the imaginary axis even right half-plane [6]. Therefore, advanced controller is required to take the place of the conventional PI controller for the control of active and reactive powers to improve the stability of the grid-connected PV power plants especially for the LVRT under grid faults.

IV. RWFNN

Though the traditional PI control has the advantage of simple structure and is easily to be implemented, it is not robust in coping with the system uncertainties such as modeling errors, parameter variations and external disturbances in practical applications. Thus, the parameters of the PI controllers obtained by trial and error are not always suitable for different operating conditions. On the other hand, the proposed RWFNN controller is essentially developed based on WFNN and RFNN. Hence, the RWFNN owns the merits of WFNN to converge quickly and to handle uncertain information and the ability of RFNN to achieve the superior dynamic modeling behavior. Therefore, due to the online learning and powerful adaptive ability of the proposed RWFNN controller, the RWFNN is proposed to replace the traditional PI controller in the grid-connected PV power plant to improve the active and reactive power control under grid faults for the weak grid conditions.

A. NETWORK STRUCTURE
The network structure of the proposed RWFNN controller is represented in Fig. 2. Besides the input and output layer, there
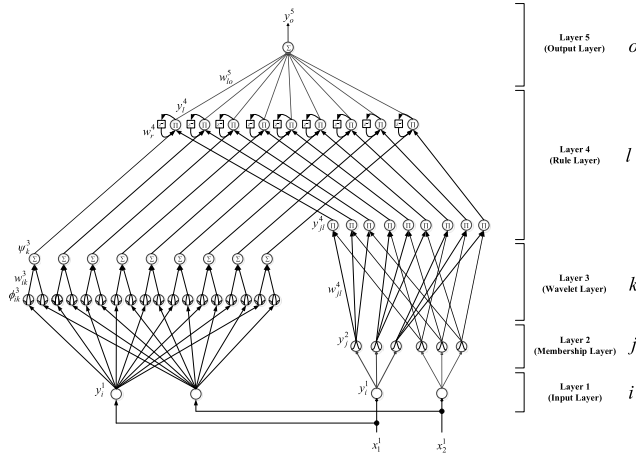
FIGURE 2. Network structure of RWFNN.

are three hidden layer in RWFNN including the membership layer, wavelet layer and rule layer. The signal propagation and the functions of each layer of RWFNN are depicted in the following:

1) LAYER 1 (INPUT LAYER)
There are two input signals in this layer. One is the tracking error e of active power or reactive power, and the other is its derivative $\dot{e}$. For every node i in this layer, its input and output are expressed as

$$net_i^1(N) = x_i^1 \tag{11}$$

$$y_i^1(N) = f_i^1(net_i^1(N)) = net_i^1(N), \quad i = 1, \ 2; \tag{12}$$

where x_i^1 is the input of *ith* node in this layer, and define x_1^1 as e while x_2^1 as $\dot{e}$; $net_i^1(N)$ expresses network inputs where superscript indicates the layer number and subscript indicates the node number; N is the number of the sampling iteration; $y_i^1(N)$ is the output of *ith* node; $f_i^1(\cdot)$ is a unity function.

2) LAYER 2 (MEMBERSHIP LAYER)
In layer 2, the outputs of layer 1 are regarded as the inputs of this layer. Moreover, the membership function of this layer adopts the Gaussian function. The relationship between the input and output of each node is described below:

$$net_j^2(N) = -\frac{(x_i^2 - m_j^2)^2}{(\sigma_j^2)^2} \tag{13}$$

$$y_j^2(N) = f_j^2(net_j^2(N)) = \exp(net_j^2(N)), \ j = 1, \ 2, \ldots, \ 6 \tag{14}$$

where $x_i^2(N) = y_i^1(N)$ is the input; m_j^2 is the mean value of Gaussian function of *jth* node; σ_j^2 is the standard deviation of Gaussian function of *jth* node; $y_j^2(N)$ is the output of *jth* node; $f_j^2(\cdot)$ is an exponential function.

3) LAYER 3 (WAVELET LAYER)
The signal propagations of wavelet layer are depicted in the following:

$$\phi_{ik}^3(x) = \frac{1}{\sqrt{|\sigma_{ik}^3|}} \left[1 - \frac{(x_i^1(N) - m_{ik}^3)^2}{(\sigma_{ik}^3)^2} \right]$$

$$\times \exp\left[\frac{-(x_i^1(N) - m_{ik}^3)^2}{2(\sigma_{ik}^3)^2} \right],$$

$$k = 1, \ 2, \ldots, \ 9 \tag{15}$$

$$\psi_k^3(N) = \sum w_{ik}^3 \phi_{ik}^3(x) \tag{16}$$

where ϕ_{ik}^3 is the input of *ith* node from layer 1 to wavelet function of *kth* node; w_{ik}^3 is the connective weight; ψ_k^3 is the output of *kth* node in the wavelet layer; σ_{ik}^3 and m_{ik}^3 express the dilation variables and translation variables of the wavelet function, respectively.

4) LAYER 4 (RULE LAYER)
This layer is composed of rule layer and recurrent layer. Each node l in this layer is denoted by $\prod$, which multiplies the input signals and outputs the result of product. Moreover, the nodes of rule layer multiply the output signals from wavelet layer and recurrent layer, and output the result of product for dynamic mapping. They are summarized in the following:

$$y_{jl}^4(N) = \prod w_{jl}^4 y_j^2, \quad l = 1, \ 2, \ldots, \ 9 \tag{17}$$

$$net_l^4(N) = y_{jl}^4 \psi_k^3 w_r^4 y_l^4(N - 1) \tag{18}$$

$$y_l^4(N) = f_l^4\left(net_l^4(N)\right) = net_l^4(N) \tag{19}$$

where $y_l^4(N)$ is the output of *lth* node in this layer; w_{jl}^4 is the connecting weight between layer 2 and layer 4; w_r^4 is the recurrent weight; $y_l^4(N - 1)$ stands for the previous output of *lth* node from this layer; $f_l^4(\cdot)$ is a unity function. The recurrent technique is adopted to incorporate a feedback loop in each node for dynamic mapping and higher sensitivity of previously obtained data.

5) LAYER 5 (OUTPUT LAYER)
The outputs of layer 4 are regarded as the inputs of this layer. Moreover, the inputs are summed up as final output of this network. It can be obtained as follows:

$$net_o^5(N) = \sum_l^9 w_{lo}^5 x_l^5(N), \quad o = 1 \tag{20}$$

$$y_o^5(N) = f_o^5(net_o^5(N)) = net_o^5(N) \tag{21}$$

where $x_l^5(N) = y_l^4(N)$ is the output from rule layer; w_{lo}^5 represents the connective weight; $y_o^5(N)$ depicts the final output of RWFNN, which means $i_{do}^* = y_o^5(N)$ or $i_{qo}^* = y_o^5(N)$ is the control effort produced by RWFNN; $f_o^5(\cdot)$ is a unity function.

B. ONLINE LEARNING ALGORITHM OF RWFNN

The detailed derivation of the online learning algorithms based on the back propagation learning rule. The objective of the back propagation algorithm is to minimize the energy function E, which is defined in the following:

$$E(N) = \frac{1}{2}(Q^* - Q)^2 = \frac{1}{2}e^2 \qquad (22)$$

where Q^* and Q are defined as the expected output and the present output of the reactive power. If it is used to control the active power, then Q^* and Q will be replaced by P^* and P, respectively. The learning algorithm is represented in the following paragraphs.

1) LAYER 5 (OUTPUT LAYER)

In layer 5, the gradient error of E in (22) with respect to the output of this layer is calculated as

$$\delta_o^5 = -\frac{\partial E}{\partial y_o^5(N)} = -\frac{\partial E}{\partial Q}\frac{\partial Q}{\partial y_o^5(N)} \qquad (23)$$

$$\Delta w_{lo}^5 = -\eta_{lo}\frac{\partial E}{\partial w_{lo}^5} = -\eta_{lo}\frac{\partial E}{\partial y_o^5(N)}\frac{\partial y_o^5(N)}{\partial w_{lo}^5} = \eta_{lo}\delta_o^5 x_l^5 \qquad (24)$$

where the factor η_{lo} is the learning rate. The connective weight w_{lo}^5 is updated in the following:

$$w_{lo}^5(N+1) = w_{lo}^5(N) + \Delta w_{lo}^5 \qquad (25)$$

2) LAYER 4 (RULE LAYER)

In layer 4, error terms need to be computed and propagated:

$$\delta_l^4 = -\frac{\partial E}{\partial y_l^4(N)} = -\left[\frac{\partial E}{\partial y_o^5(N)}\right]\frac{\partial y_o^5(N)}{\partial y_l^4} = \delta_o^5 w_{lo}^5 \qquad (26)$$

$$\delta_{jl}^4 = -\frac{\partial E}{\partial y_{jl}^4(N)} = -\left[\frac{\partial E}{\partial y_o^5(N)}\frac{\partial y_o^5(N)}{\partial y_l^4(N)}\right]\frac{\partial y_l^4(N)}{\partial y_{jl}^4(N)}$$
$$= \delta_l^4 \phi_k^3 w_r^4 y_l^4(N-1) \qquad (27)$$

$$\Delta w_r^4 = -\eta_r \frac{\partial E}{\partial w_r^4} = -\eta_r\left[\frac{\partial E}{\partial y_o^5(N)}\frac{\partial y_o^5(N)}{\partial y_l^4(N)}\right]\frac{\partial y_l^4(N)}{\partial w_r^4(N)}$$
$$= \eta_r \delta_l^4 \psi_k^3 y_{jl}^4 y_l^4(N-1) \qquad (28)$$

where the factor η_r is the learning rate. The recurrent weight w_r^4 is updated in the following:

$$w_r^4(N+1) = w_r^4(N) + \Delta w_r^4 \qquad (29)$$

3) LAYER 2 (MEMBERSHIP LAYER)

In layer 2, error term need to be propagated and computed:

$$\delta_j^2 = -\frac{\partial E}{\partial net_j^2} = -\left[\frac{\partial E}{\partial y_{jl}^4(N)}\right]\frac{\partial y_{jl}^4(N)}{\partial y_j^2(N)}\frac{\partial y_j^2(N)}{\partial net_j^2(N)} = \sum_{jl}\delta_{jl}^4 y_{jl}^4 \qquad (30)$$

By means of the chain rule, the mean value and standard deviation of the Gaussian function can be computed by the following equations:

$$\Delta m_j^2 = -\eta_m\frac{\partial E}{\partial m_j^2} = -\eta_m\left[\frac{\partial E}{\partial net_j^2(N)}\right]\frac{\partial net_j^2(N)}{\partial m_j^2(N)}$$
$$= \eta_m \delta_j^2 \frac{2(x_i^2 - m_j^2)}{(\sigma_j^2)^2} \qquad (31)$$

$$\Delta \sigma_j^2 = -\eta_\sigma\frac{\partial E}{\partial \sigma_j^2} = -\eta_\sigma\left[\frac{\partial E}{\partial net_j^2(N)}\right]\frac{\partial net_j^2(N)}{\partial \sigma_j^2(N)}$$
$$= \eta_\sigma \delta_j^2 \frac{2(x_i^2 - m_j^2)^2}{(\sigma_j^2)^3} \qquad (32)$$

where the factors η_m and η_σ are the learning rates. The m_j^2 and σ_j^2 are updated according to the following equations:

$$m_j^2(N+1) = m_j^2(N) + \Delta m_j^2 \qquad (33)$$
$$\sigma_j^2(N+1) = \sigma_j^2(N) + \Delta \sigma_j^2 \qquad (34)$$

Due to the uncertainties of the system, the exact calculation of the sensitivity of the system $\partial Q/\partial y_o^5(N)$ cannot be determined exactly. Therefore, for the purpose of solving this problem, the delta adaptation law is adopted to increase the online learning speed of the network parameters [20]:

$$\delta_o^5 \cong e + \dot{e} \qquad (35)$$

C. CONVERGENCE ANALYSIS OF RWFNN

In order to make the RWFNN function effectively, a Lyapunov function is used to prove the convergence of the tracking errors [27]. The specific learning rate coefficients for the training of the network parameters are obtained from the following convergence analysis to guarantee the convergence of reactive power control.

The energy function shown in (22) is regarded as a discrete-type Lyapunov function. Hence, the variation of the Lyapunov function is described as:

$$\Delta E(N) = E(N+1) - E(N) \qquad (36)$$

Linearized model [28] of the Lyapunov function is obtained via (24), (28), (31) and (32) in the following:

$$E(N+1)$$
$$= E(N) + \Delta E(N)$$
$$\approx E(N) + \sum_{o=1}^{1}\sum_{l=1}^{9}\left[\frac{\partial E(N)}{\partial w_{lo}^5}\Delta w_{lo}^5\right] + \sum_{r=1}^{9}\left[\frac{\partial E(N)}{\partial w_r^4}\Delta w_r^4\right]$$
$$+ \sum_{j=1}^{6}\left[\frac{\partial E(N)}{\partial m_j^2}\Delta m_j^2 + \frac{\partial E(N)}{\partial \sigma_j^2}\Delta \sigma_j^2\right]$$
$$= \frac{1}{4}E(N) - \eta_{lo}\sum_{o=1}^{1}\sum_{l=1}^{9}\left[\frac{\partial E(N)}{\partial w_{lo}^5}\right]^2$$
$$+ \frac{1}{4}E(N) - \eta_r\sum_{r=1}^{9}\left[\frac{\partial E(N)}{\partial w_r^4(N)}\right]^2$$
$$+ \frac{1}{4}E(N) - \eta_m\sum_{j=1}^{6}\left[\frac{\partial E(N)}{\partial m_j^2(N)}\right]^2$$
$$+ \frac{1}{4}E(N) - \eta_\sigma\sum_{j=1}^{6}\left[\frac{\partial E(N)}{\partial \sigma_j^2(N)}\right]^2 \qquad (37)$$

where Δw_{lo}^5, Δw_r^4, Δm_j^2 and $\Delta \sigma_j^2$ express the variations of the connective weights, the means and the standard deviations.

If the learning rate coefficients of the RWFNN are designed as:

$$\eta_{lo} = \frac{E(N)}{4 \left[\sum\limits_{o=1}^{1} \sum\limits_{l=1}^{9} \left[\frac{\partial E(N)}{\partial w_{lo}^5(N)} \right]^2 + \varepsilon \right]} \tag{38}$$

$$\eta_{r} = \frac{E(N)}{4 \left[\sum\limits_{r=1}^{9} \left[\frac{\partial E(N)}{\partial w_{r}^4(N)} \right]^2 + \varepsilon \right]} \tag{39}$$

$$\eta_{m} = \frac{E(N)}{4 \left[\sum\limits_{j=1}^{6} \left[\frac{\partial E(N)}{\partial m_{j}^2(N)} \right]^2 + \varepsilon \right]} \tag{40}$$

$$\eta_{\sigma} = \frac{E(N)}{4 \left[\sum\limits_{j=1}^{6} \left[\frac{\partial E(N)}{\partial \sigma_{j}^2(N)} \right]^2 + \varepsilon \right]} \tag{41}$$

where ε is a positive constant. Equation (37) can be rewritten in the following:

$$
\begin{aligned}
E(N+1) \approx & \frac{E(N)\varepsilon}{4 \left[\sum\limits_{o=1}^{1} \sum\limits_{l=1}^{9} \left[\frac{\partial E(N)}{\partial w_{lo}^5(N)} \right]^2 + \varepsilon \right]} \\
& + \frac{E(N)\varepsilon}{4 \left[\sum\limits_{r=1}^{9} \left[\frac{\partial E(N)}{\partial w_{r}^4(N)} \right]^2 + \varepsilon \right]} \\
& + \frac{E(N)\varepsilon}{4 \left[\sum\limits_{j=1}^{6} \left[\frac{\partial E(N)}{\partial m_{j}^2(N)} \right]^2 + \varepsilon \right]} \\
& + \frac{E(N)\varepsilon}{4 \left[\sum\limits_{j=1}^{6} \left[\frac{\partial E(N)}{\partial \sigma_{j}^2(N)} \right]^2 + \varepsilon \right]} \\
< & \frac{E(N)}{4} + \frac{E(N)}{4} + \frac{E(N)}{4} + \frac{E(N)}{4} = E(N) \quad (42)
\end{aligned}
$$

Finally, the convergence of the proposed RWFNN controller is guaranteed according to (22) and (42). Thus, the convergence the reactive power control of the PV power plant can be pledged.

V. DESIGN AND SIMULATION

Regarding the design of the RWFNN, there are 2, 6, 27, 18 and 1 neurons in the input, membership, wavelet, rule and output layers of the adopted RWFNNs. In general, if more neurons of the membership, wavelet and rule layers are adopted, better control performance can be obtained. However, increase the numbers of neurons will increase the execution time. Thus, 6, 27 and 18 neurons are adopted at the membership, wavelet and rule layers by empirical rules to achieve fast responses of the PV system and to reduce the execution time. Moreover, considering the performance of power tracking, the proportional and integral gains of the PI controllers for the tracking of active and reactive powers are obtained by trial and error, and the proportional gain is 0.5 and the integral gain is 45. Furthermore, to compare the performance of the proposed RWFNN controller, an FNN controller proposed in [29] is also considered in the simulation. In this study, two test cases for low SCR value, which is 3, are configured as follows: In Case 1, inverter output power is set at 1.7 kW and three-phase voltages of the grid are set at 1 pu; then the voltage dip is set to be 0.3 pu at 1.0 sec owing to grid fault. In Case 2, inverter output power is set at 1.7 kW and three-phase voltages of the grid are set at 1 pu; then the voltage dip is set to be 0.5 pu at 1.0 sec owing to grid fault. In addition, according to the LVRT requirements, the grid-connected inverters should withstand and remain connected during certain grid faults. Therefore, in order to comply with the LVRT requirements, usually the DC/DC converter has to stop tracking the maximum power point (MPP) of PV panel to maintain the active power balance between the PV panel and grid-connected three-phase smart inverter. Therefore, during the grid fault, the PV power plant is not operated at the MPP owing to the active power control [27]. Additionally, for the interleaved DC/DC converter, the values of input capacitor, three filter inductors and output capacitor are 1175 μF, 0.52 mH and 1175 μF respectively. For the NPC smart inverter, the values of capacitors of DC bus, and the values of inductors and capacitors of three output filters are 3760 μF, 1.6 mH and 10 μF respectively.

The simulation results of Case 1 are shown in Fig. 3, where V_{pcc_q} is the q-axis voltage of the positive sequence of three-phase voltage at the PCC and equal to $\sqrt{2}\left|V_p^+\right|$. Initially the three-phase voltages of the PCC V_{pcc_a}, V_{pcc_b} and V_{pcc_c} are 1.067 pu and V_{pcc_q} is 191.665 V. The output active power and reactive power of the PV power plant are 1.7 *kW* and 0 *kVAR* respectively. Then the grid fault occurs at 1.0 sec with voltage dip 0.3 pu, the resulted three-phase voltages of the PCC become 0.829 pu and V_{pcc_q} is 148.913V owing to the grid impedance Z_{grid}; V_{dip} at the PCC is 0.171 pu. In accordance with the LVRT requirements, the output active power and reactive powers of the PV power plant become 1.324 *kW* and 0.482 *kVAR* respectively. The tracking responses of the active and reactive powers using the PI controllers are shown in Fig. 3(a) where unstable responses with both active and reactive powers oscillating are obtained due to weak grid. Moreover, the tracking responses of the active and reactive powers using the FNN controllers are provided in Fig. 3(b) where the unstable responses with both active and reactive powers oscillating are improved by the FNN. Furthermore, the tracking responses of active and reactive powers using the proposed RWFNN controllers are shown in Fig. 3(c) where much smooth tracking responses are achieved for both the active and reactive powers with decaying oscillating phenomena. According to the simulation results by using the PI, FNN and RWFNN controllers which are shown in Figs. 3(a), 3(b) and 3(c), the peak-to-peak values of the V_{pcc_q} using the PI, FNN and RWFNN controllers in the
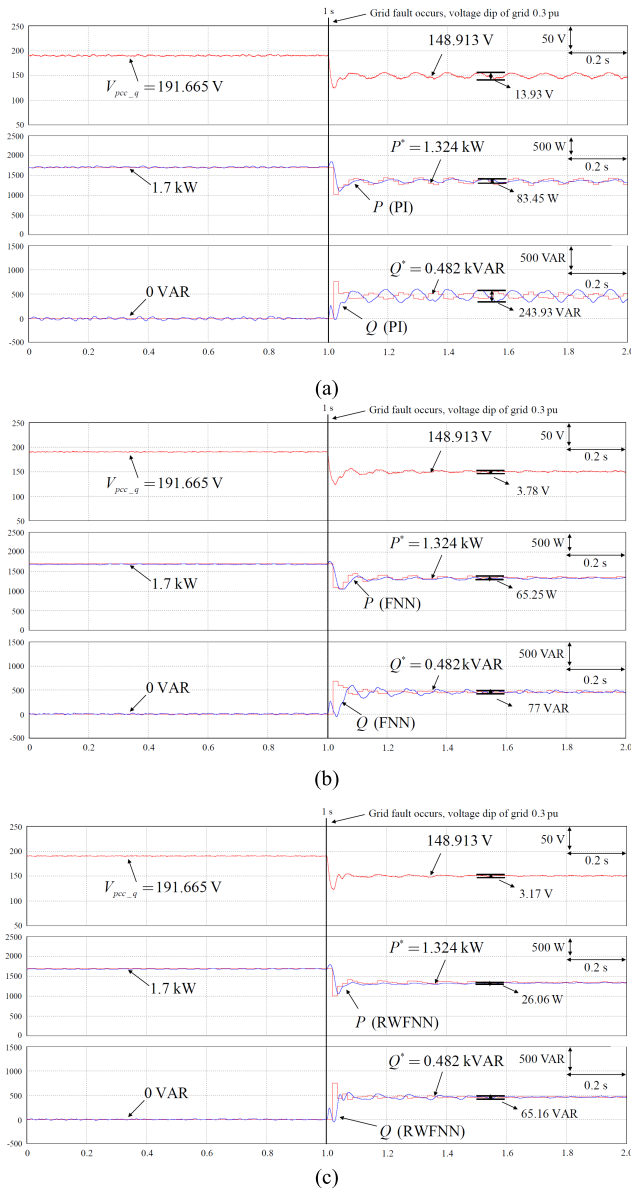
FIGURE 3. Simulation results of Case 1. (a) Tracking of active and reactive power using PI controllers, (b) Tracking of active and reactive power using FNN controllers, (c) Tracking of active and reactive power using RWFNN controllers.
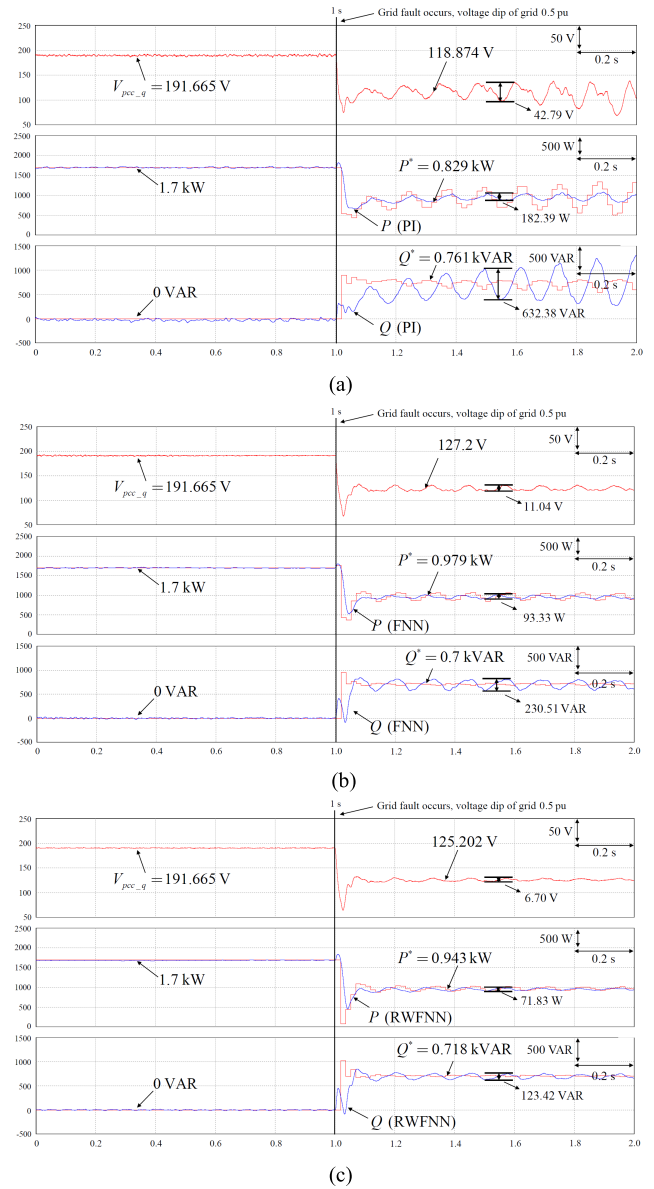

FIGURE 4. Simulation results of Case 2. (a) Tracking of active and reactive power using PI controllers, (b) Tracking of active and reactive power using FNN controllers, (c) Tracking of active and reactive power using RWFNN controllers.

time interval 1.5 s to 1.6 s are 13.93 V, 3.78 V and 3.17 V respectively. The active power oscillatory responses using the PI, FNN and RWFNN controllers in the time interval 1.5 s to 1.6 s are 83.45 W, 65.25 W and 26.06 W respectively. The reactive power oscillatory responses using the PI, FNN and RWFNN controllers in the time interval 1.5 s to 1.6 s are 243.93 VAR, 77 VAR and 65.16 VAR respectively.

The simulation results of Case 2 are shown in Fig. 4. Initially the three-phase voltages of the PCC V_{pcc_a}, V_{pcc_b} and V_{pcc_c} are also 1.067 pu and the output active power and reactive powers of the PV power plant are 1.7 kW and 0 kVAR respectively. Then the grid fault occurs at 1.0 sec with voltage dip 0.5 pu, the resulted three-phase voltages of the PCC become 0.662 pu and V_{pcc_q} is 118.874V owing to the grid

impedance Z_{grid}; V_{dip} at the PCC is 0.338 pu. According to the LVRT requirements, the output active power and reactive powers of the PV power plant become 0.829 *kW* and 0.761 *kVAR* respectively. The tracking responses of active and reactive powers using the PI controllers are shown in Fig. 4(a) where much more unstable responses with both active and reactive powers oscillating due to weak grid are obtained. Moreover, the tracking responses of active and reactive powers using the FNN controllers are shown in Fig. 4(b) where the unstable responses with both active and reactive powers oscillating are improved by the FNN. Furthermore, the tracking responses of the active and reactive powers using the RWFNN controllers are shown in Fig. 4(c) where much smooth tracking responses are also achieved for both the active and

TABLE 1. Comparison of peak-to-peak values of oscillatory responses of PV power plant using PI, FNN and RWFNN in time interval 1.5 s to 1.6 s of simulation.

Controllers	Simulation					
	PI		FNN		RWFNN	
Responses	Case 1	Case 2	Case 1	Case 2	Case 1	Case 2
V_{pcc_q} (V)	13.93 (7%)	42.79 (24%)	3.78 (2%)	11.04 (6%)	3.17 (2%)	6.70 (4%)
P(W)	83.45 (4%)	182.39 (9%)	65.25 (3%)	93.33 (5%)	26.06 (1%)	71.83 (4%)
Q(VAR)	243.93 (12%)	632.38 (32%)	77 (4%)	230.51 (12%)	65.16 (3%)	123.42 (6%)

reactive powers with reduced oscillations. According to the simulation results by using the PI, FNN and RWFNN controllers which are shown in Figs. 4(a), 4(b) and 4(c), the peak-to-peak values of the V_{pcc_q} using the PI, FNN and RWFNN controllers in the time interval 1.5 s to 1.6 s are 42.79 V, 11.04 V and 6.7 V respectively. The active power oscillatory responses using the PI, FNN and RWFNN controllers in the time interval 1.5 s to 1.6 s are 182.39 W, 93.33 W and 71.83 W respectively. The reactive power oscillatory responses using the PI, FNN and proposed RWFNN controllers in the time interval 1.5 s to 1.6 s are 632.38 VAR, 230.51 VAR and 123.42 VAR respectively.

The comparison of the peak-to-peak values of the oscillatory responses of the PV power plant using the PI, FNN and RWFNN controllers in the time interval 1.5 s to 1.6 s of the simulation are provided in Table 1. According to Table 1, the peak-to-peak values of the oscillatory responses of the PV power plant using the proposed RWFNN controllers are much reduced at all test conditions. The percentages of the oscillatory amplitudes to the steady-state values of V_{pcc_q}, active power and reactive power responses have also been indicated in Table 1.

VI. EXPERIMENTAL SET-UP AND EXPERIMENTATION

The photos of the PV power system, including two DSP TMS320F28335 control boards, are shown in Figs. 5(a) and 5(b). The interleaved DC/DC converter, three-level NPC inverter and PV simulator are shown in Fig. 5(a). In this study, the PV panel is emulated by using Chroma 62100H-600S. The open circuit voltage and short circuit current of the emulated PV panel are set as 375.9 V and 6.518 A respectively. Moreover, the voltage, current and power output at the MPP of the PV panel are set as 324 V, 6.173 A and 2 kW. The RL impedance, Y-Y transformer and grid emulator are shown in Fig. 5(b). An emulated three-phase overhead line is connected between the PCC and the grid. The emulated grid impedances Z_{grid} are built in the RL impedance indicated in Fig. 5(b) which are 1.9021+j8.4332Ω, 1.8854+ j8.2031Ω and 1.9141+j7.9091Ω respectively for a weak grid with SCR 3. Owing to the allowed error of the manufacture, the real three-phase grid impedances are deviated from the designed Z_{grid} which is 1.9565+ j7.8258Ω. The cut-off frequency f_c of the output filter is 1.258 kHz. Moreover, the DC bus voltage command V_{dc}^* is set at 450 V. Furthermore, the switching frequency of the interleaved DC/DC converter and three-level NPC inverter are both set to be 16 kHz.
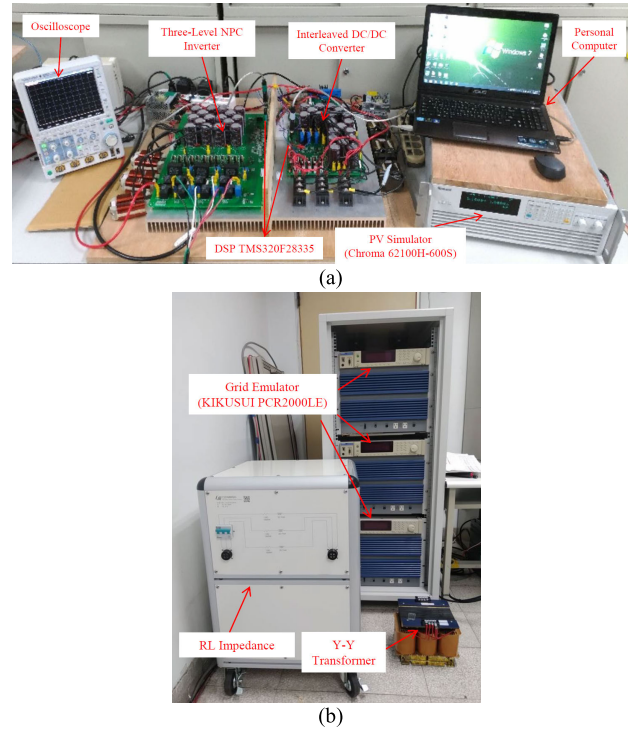

(a)

(b)

FIGURE 5. Photos of experimental set–up. (a) Interleaved DC/DC converter, three-level NPC inverter and PV simulator, (b) RL Impedance, Y-Y transformer and grid emulator.

In addition, the sampling frequency 1 kHz is adopted for the control algorithms of both stages. The proportional gain and the integral gain of the PI controller are also 0.5 and 45 respectively.
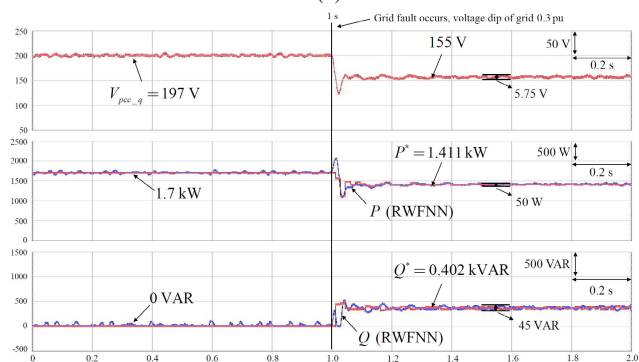
The experimental results of Case 1 are shown in Fig. 6. Initially the three-phase voltages of the PCC V_{pcc_a}, V_{pcc_b} and V_{pcc_c} are 1.097 pu and V_{pcc_q} is 197 V. The output active power and reactive power of the PV power plant are 1.7 *kW* and 0 *kVAR* respectively. Then the grid fault occurs at 1.0 sec with voltage dip 0.3 pu, the resulted three-phase voltages of the PCC become 0.863 pu and V_{pcc_q} is 155 V owing to the grid impedance Z_{grid}; V_{dip} at the PCC is 0.137 pu. According to the LVRT requirements, the output active power and reactive powers of the PV power plant become 1.411 *kW* and 0.402 *kVAR* respectively. The tracking responses of active and reactive powers using the PI controllers are shown in Fig. 6(a) where unstable responses with both active and reactive powers oscillating are obtained due to weak grid. Moreover, the upper half DC bus voltage V_{d1} and the lower half DC bus voltage V_{d2} with the active and reactive powers using the PI controllers are provided in Fig. 6(b). On the other hand, the tracking responses of active and reactive powers using the RWFNN controllers are shown in Fig. 6(c) where much smooth tracking responses are achieved for both the active and reactive powers. In the time interval 1.5 s to 1.6 s, the peak-to-peak values of the V_{pcc_q}, active power and reactive power oscillatory responses have been reduced from 11.25 V to 5.75 V, 97.5 W to 50 W and 147.5 VAR to 45 VAR, respectively, by using the proposed RWFNN. Furthermore,
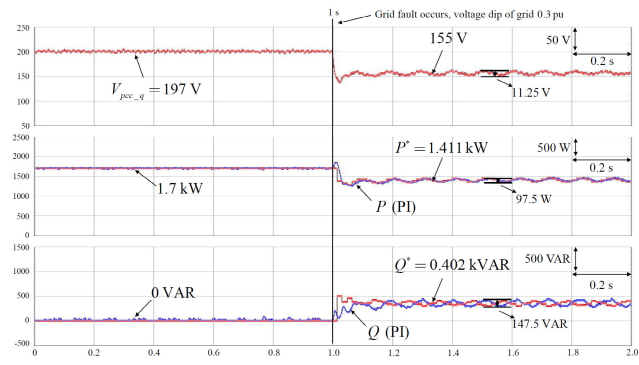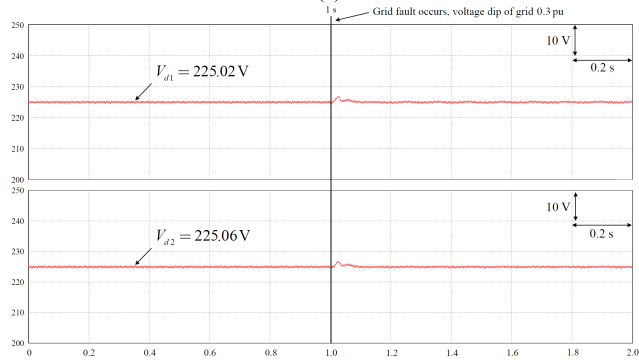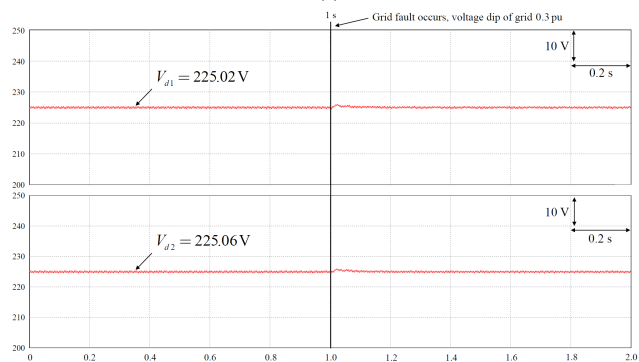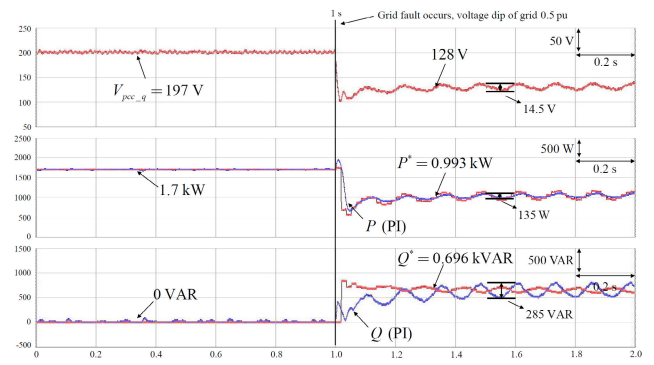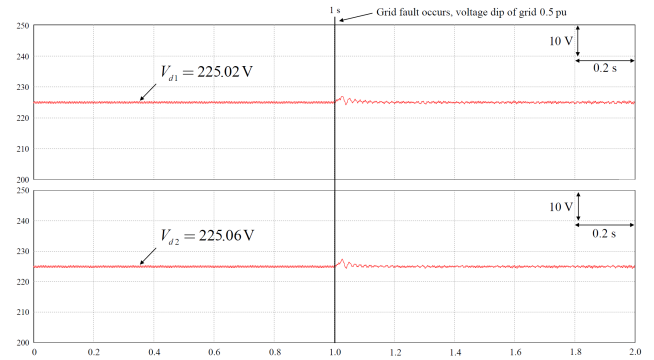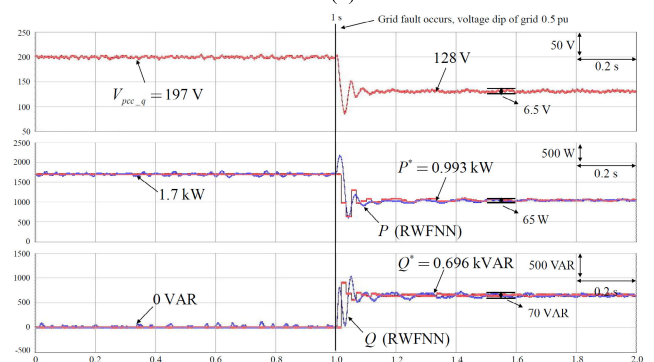
FIGURE 6. Experimental results of Case 1: (a) Tracking of active and reactive power using PI controllers, (b) Upper half DC bus voltage V_{d1} and lower half DC bus voltage V_{d2} regulated by PI controllers, (c) Tracking of active and reactive power using RWFNN controllers, (d) Upper half DC bus voltage V_{d1} and lower half DC bus voltage V_{d2} regulated by RWFNN controllers.

FIGURE 7. Experimental results of Case 2: (a) Tracking of active and reactive power using PI controllers, (b) Upper half DC bus voltage V_{d1} and lower half DC bus voltage V_{d2} regulated by PI controllers, (c) Tracking of active and reactive power using RWFNN controllers, (d) Upper half DC bus voltage V_{d1} and lower half DC bus voltage V_{d2} regulated by RWFNN controllers.
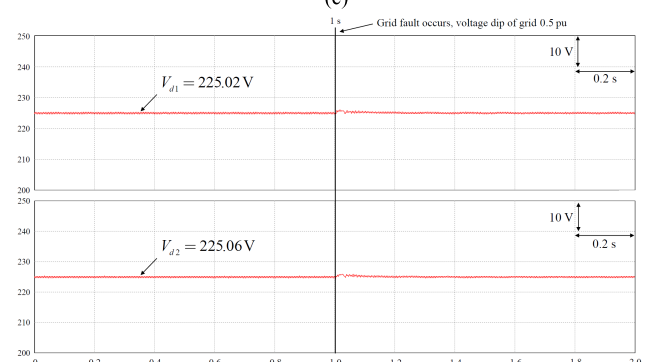
FIGURE 8. Enlarged experimental results of Case 1 in interval 1 to 1.6 s. (a) Tracking of active and reactive power using PI controllers, (b) Tracking of active and reactive power using RWFNN controllers.
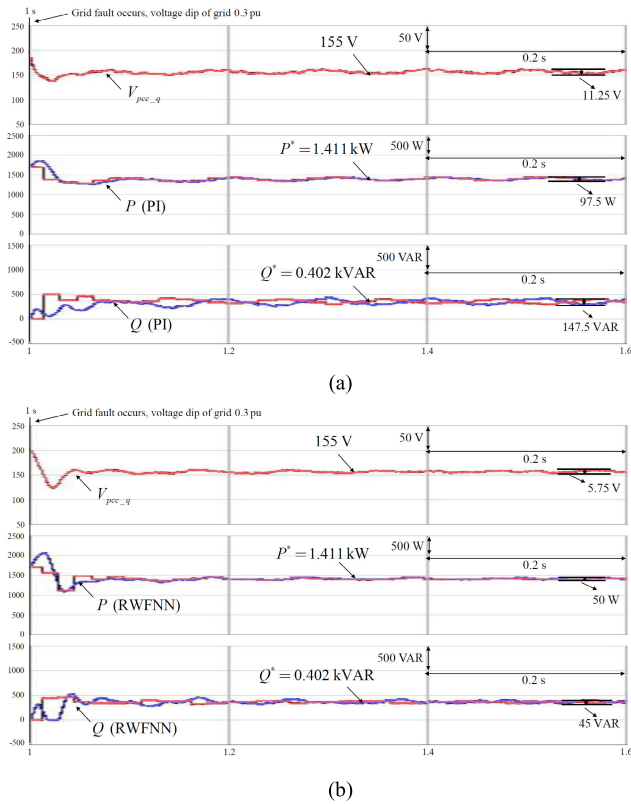

FIGURE 9. Enlarged experimental results of Case 2 in interval 1 to 1.6 s. (a) Tracking of active and reactive power using PI controllers, (b) Tracking of active and reactive power using RWFNN controllers.

the upper half DC bus voltage V_{d1} and the lower half DC bus voltage V_{d2} with the active and reactive powers using the proposed RWFNN controllers are provided in Fig. 6(d). Comparing to the Fig. 6(b), since the three-phase voltage commands V_a^*, V_b^*, V_c^* are affected by the current commands i_{do}^* and i_{qo}^* using PI or the proposed RWFNN controllers, the upper half DC bus voltage V_{d1} and the lower half DC bus voltage V_{d2} can be also improved by the proposed RWFNN controllers at the moment of the grid fault.

The experimental results of Case 2 are shown in Fig. 7. Initially the three-phase voltages of the PCC V_{pcc_a}, V_{pcc_b} and V_{pcc_c} are also 1.097 pu and V_{pcc_q} is 197 V. The output active power and reactive powers of the PV power plant are 1.7 kW and 0 kVAR respectively. Then the grid fault occurs at 1.0 sec with voltage dip 0.5 pu, the resulted three-phase voltages of the PCC become 0.713 pu and V_{pcc_q} is 128 V owing to the grid impedance Z_{grid}; V_{dip} at the PCC is 0.287 pu. According to the LVRT requirements, the output active power and reactive powers of the PV power plant become 0.993 kW and 0.696 kVAR respectively. The tracking responses of active and reactive powers using the PI controllers are shown in Fig. 7(a) where seriously unstable responses with both active and reactive powers oscillating due to weak grid are obtained. Moreover, the upper half DC bus voltage V_{d1} and the lower half DC bus voltage V_{d2} with the active and reactive powers using the PI controllers are provided in Fig. 7(b). On the other hand, the tracking responses of active and reactive powers
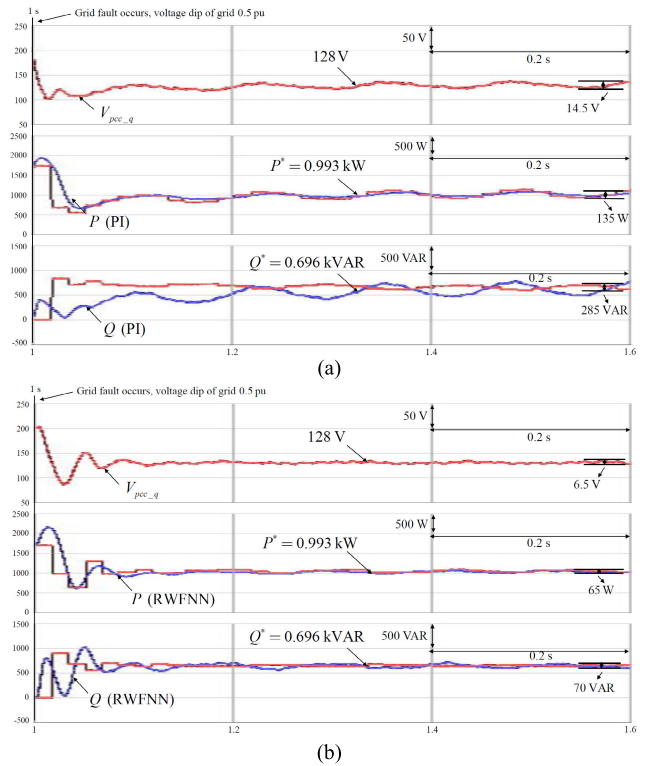
using the RWFNN controllers are shown in Fig. 7(c) where much smooth tracking responses are also achieved for both the active and reactive powers. In the time interval 1.5 s to 1.6 s, the peak-to-peak values of the V_{pcc_q}, active power and reactive power oscillatory responses have been reduced from 14.5 V to 6.5 V, 135 W to 65 W and 285 VAR to 70 VAR, respectively, by using the proposed RWFNN. Furthermore, the upper half DC bus voltage V_{d1} and the lower half DC bus voltage V_{d1} with the active and reactive powers using the proposed RWFNN controllers are provided in Fig. 7(d). Comparing to the Fig. 7(b), the upper half DC bus voltage V_{d1} and the lower half DC bus voltage V_{d2} can be also improved by the proposed RWFNN controllers at the moment of the grid fault due to the powerful online learning and parallel processing capabilities of the RWFNN.

To better understand the performance comparison between PI and RWFNN, the responses in the time interval 1 to 1.6s of the experimental results of Case 1 and 2 as shown in Figs. 6(a), 6(c), 7(a) and 7(c) are enlarged in Figs. 8(a), 8(b), 9(a) and 9(b). According to the experimental results shown in Figs. 8(a) and 9(a), since the conventional PI controller is not robust in dealing with the system uncertainties such as external disturbances and parameter variations, the tracking responses of the active and reactive power are poor. On the other hand, the proposed RWFNN combines the advantage of the RNN to achieve the dynamic modeling behavior, the advantage of WNN to converge quickly with high precision, and the advantage of FNN to handle uncertain

TABLE 2. Comparison of peak-to-peak values of oscillatory responses of PV power plant using PI and RWFNN in time interval 1.5 s to 1.6 s of experimentation.

Controllers	Experimentation			
	PI		RWFNN	
Responses	Case 1	Case 2	Case 1	Case 2
V_{pcc_q}(V)	11.25 (6%)	14.5 (8%)	5.75 (3%)	6.5 (4%)
P(W)	97.5 (5%)	135 (7%)	50 (3%)	65 (3%)
Q(VAR)	147.5 (7%)	285 (14%)	45 (2%)	70 (4%)

information. Therefore, the proposed RWFNN controller can deal with all different operating conditions and achieve the best transient and steady-state performance of the system. Hence, the PV power plant using the proposed RWFNN controllers can much improve the tracking responses of the active and reactive power as shown in Figs. 8(b) and 9(b). In addition, the comparison of the peak-to-peak values of the oscillatory responses of the PV power plant using the PI and RWFNN controllers in the time interval 1.5 s to 1.6 s are provided in Table 2. According to Table 2, the peak-to-peak values of the oscillatory responses of the PV power plant using the proposed RWFNN controllers are much reduced at all test conditions. The percentages of the oscillatory amplitudes to the steady-state values of V_{pcc_q}, active power and reactive power responses have also been indicated in Table 2.

VII. CONCLUSION

In this study, an intelligent control method using RWFNN was successfully developed to improve the LVRT performance of a two-stage PV power plant under grid faults for the weak grid conditions. An emulated weak grid is connected between the PCC of the PV power plant and the grid, and the resulted SCR is only 3. Since low SCR values impose serious problems in terms of voltage stability and power quality especially under grid faults for the output active and reactive powers tracking of a PV power plant, the RWFNN controller was developed to replace the traditional PI controller to improve the transient stability during grid faults for the weak grid conditions. From both the simulation and experimental results, much smooth tracking responses can be achieved with reduced oscillations for the tracking of active and reactive power commands, which are obtained according to the LVRT requirements, by using the RWFNN controller due to its powerful online learning and parallel processing capabilities. Though only the E.ON standard is adopted in this study to generate the active and reactive power commands according to the LVRT requirements under various grid faults, the proposed RWFNN controller can improve the instability phenomena caused by the weak grid for any adopted LVRT standard to generate the active and reactive power commands.

REFERENCES

[1] S. Liu, P. X. Liu, and X. Wang, "Stability analysis of grid-interfacing inverter control in distribution systems with multiple photovoltaic-based distributed generators," *IEEE Trans. Ind. Electron.*, vol. 63, no. 12, pp. 7339–7348, Dec. 2016.

[2] Z. Wang, B. Chen, J. Wang, and M. M. Begovic, "Stochastic DG placement for conservation voltage reduction based on multiple replications procedure," *IEEE Trans. Power Del.*, vol. 30, no. 3, pp. 1039–1047, Jun. 2015.

[3] J. Han, S. Khushalani-Solanki, J. Solanki, and J. Liang, "Adaptive critic design-based dynamic stochastic optimal control design for a microgrid with multiple renewable resources," *IEEE Trans. Smart Grid*, vol. 6, no. 6, pp. 2694–2703, Nov. 2015.

[4] S. Alepuz, S. Busquets-Monge, J. Bordonau, J. A. Martinez-Velasco, C. A. Silva, J. Pontt, and J. Rodriguez, "Control strategies based on symmetrical components for grid-connected converters under voltage dips," *IEEE Trans. Ind. Electron.*, vol. 56, no. 6, pp. 2162–2173, Jun. 2009.

[5] C.-Y. Tang, Y.-T. Chen, and Y.-M. Chen, "PV power system with multimode operation and low-voltage ride-through capability," *IEEE Trans. Ind. Electron.*, vol. 62, no. 12, pp. 7524–7533, Dec. 2015.

[6] S. Mortazavian and Y. A.-R.-I. Mohamed, "Dynamic analysis and improved LVRT performance of multiple DG units equipped with grid-support functions under unbalanced faults and weak grid conditions," *IEEE Trans. Power Electron.*, vol. 33, no. 10, pp. 9017–9032, Oct. 2018.

[7] M. A. Shuvra and B. Chowdhury, "Distributed dynamic grid support using smart PV inverters during unbalanced grid faults," *IET Renew. Power Gener.*, vol. 13, no. 4, pp. 598–608, Mar. 2019.

[8] X. Chen, Y. Zhang, S. Wang, J. Chen, and C. Gong, "Impedance-phased dynamic control method for grid-connected inverters in a weak grid," *IEEE Trans. Power Electron.*, vol. 32, no. 1, pp. 274–283, Jan. 2017.

[9] D. Wu, G. Li, M. Javadi, A. M. Malyscheff, M. Hong, and J. N. Jiang, "Assessing impact of renewable energy integration on system strength using site-dependent short circuit ratio," *IEEE Trans. Sustain. Energy*, vol. 9, no. 3, pp. 1072–1080, Jul. 2018.

[10] S. M. Alizadeh, C. Ozansoy, and A. Kalam, "Investigation into the impact of PCC parameters on voltage stability in a DFIG wind farm," in *Proc. Australas. Universities Power Eng. Conf. (AUPEC)*, Nov. 2017, pp. 1–6.

[11] L.-J. Cai and I. Erlich, "Doubly fed induction generator controller design for the stable operation in weak grids," *IEEE Trans. Sustain. Energy*, vol. 6, no. 3, pp. 1078–1084, Jul. 2015.

[12] Q. Jia, G. Yan, Y. Cai, and Y. Li, "Small signal stability analysis of paralleled inverters for multiple photovoltaic generation units connected to weak grid," in *Proc. Int. Conf. Renew. Power Gener. (RPG)*, Jilin, China, 2017, pp. 1–6.

[13] S.-Y. Chen, Y.-H. Hung, and S.-S. Gong, "Speed control of vane-type air motor servo system using proportional-integral-derivative-based fuzzy neural network," *Int. J. Fuzzy Syst.*, vol. 18, no. 6, pp. 1065–1079, Dec. 2016.

[14] F.-J. Lin and R.-J. Wai, "Sliding-mode-controlled slider-crank mechanism with fuzzy neural network," *IEEE Trans. Ind. Electron.*, vol. 48, no. 1, pp. 60–70, Feb. 2001.

[15] Y. Li, H.-L. Wei, and S. A. Billings, "Identification of time-varying systems using multi-wavelet basis functions," *IEEE Trans. Control Syst. Technol.*, vol. 19, no. 3, pp. 656–663, May 2011.

[16] J. P. S. Catalao, H. M. I. Pousinho, and V. M. F. Mendes, "Hybrid Wavelet-PSO-ANFIS approach for short-term electricity prices forecasting," *IEEE Trans. Power Syst.*, vol. 26, no. 1, pp. 137–144, Feb. 2011.

[17] C.-H. Lu, "Wavelet fuzzy neural networks for identification and predictive control of dynamic systems," *IEEE Trans. Ind. Electron.*, vol. 58, no. 7, pp. 3046–3058, Jul. 2011.

[18] M. Shahriari-kahkeshi and F. Sheikholeslam, "Adaptive fuzzy wavelet network for robust fault detection and diagnosis in non-linear systems," *IET Control Theory Appl.*, vol. 8, no. 15, pp. 1487–1498, Oct. 2014.

[19] S. H. Park and S. I. Han, "Robust-tracking control for robot manipulator with deadzone and friction using backstepping and RFNN controller," *IET Control Theory Appl.*, vol. 5, no. 12, pp. 1397–1417, Aug. 2011.

[20] F.-J. Lin, I.-F. Sun, K.-J. Yang, and J.-K. Chang, "Recurrent fuzzy neural cerebellar model articulation network fault-tolerant control of six-phase permanent magnet synchronous motor position servo drive," *IEEE Trans. Fuzzy Syst.*, vol. 24, no. 1, pp. 153–167, Feb. 2016.

[21] Y.-Y. Lin, J.-Y. Chang, and C.-T. Lin, "Identification and prediction of dynamic systems using an interactively recurrent self-evolving fuzzy neural network," *IEEE Trans. Neural Netw. Learn. Syst.*, vol. 24, no. 2, pp. 310–321, Feb. 2013.

[22] T. Mai and Y. Wang, "Adaptive force/motion control system based on recurrent fuzzy wavelet CMAC neural networks for condenser cleaning crawler-type mobile manipulator robot," *IEEE Trans. Control Syst. Technol.*, vol. 22, no. 5, pp. 1973–1982, Sep. 2014.

[23] S. Ganjefar and M. Tofighi, "Single-hidden-layer fuzzy recurrent wavelet neural network: Applications to function approximation and system identification," *Inf. Sci.*, vol. 294, pp. 269–285, Feb. 2015.

[24] A. Q. Al-Shetwi, M. Sujod, and N. L. Ramli, "A review of the fault ride through requirements in different grid codes concerning penetration of PV system to the electric power network," *ARPN J. Eng. Appl. Sci.*, vol. 10, no. 21, pp. 9906–9912, Nov. 2015.

[25] *Grid Code High and Extra High Voltage*, E.ON Netz GmbH, Bayreuth, Germany, Apr. 2006.

[26] F.-J. Lin, K.-C. Lu, and B.-H. Yang, "Recurrent fuzzy cerebellar model articulation neural network based power control of a single-stage three-phase grid-connected photovoltaic system during grid faults," *IEEE Trans. Ind. Electron.*, vol. 64, no. 2, pp. 1258–1268, Feb. 2017.

[27] F.-J. Lin, K.-C. Lu, T.-H. Ke, B.-H. Yang, and Y.-R. Chang, "Reactive power control of three-phase grid-connected PV system during grid faults using Takagi–Sugeno–Kang probabilistic fuzzy neural network control," *IEEE Trans. Ind. Electron.*, vol. 62, no. 9, pp. 5516–5528, Sep. 2015.

[28] R.-J. Wai and C.-M. Liu, "Design of dynamic Petri recurrent fuzzy neural network and its application to path-tracking control of nonholonomic mobile robot," *IEEE Trans. Ind. Electron.*, vol. 56, no. 7, pp. 2667–2683, Jul. 2009.

[29] J. S. Lim, "Finding features for real-time premature ventricular contraction detection using a fuzzy neural network system," *IEEE Trans. Neural Netw.*, vol. 20, no. 3, pp. 522–527, Mar. 2009.

FAA-JENG LIN (Fellow, IEEE) received the B.S. and M.S. degrees in electrical engineering from National Cheng Kung University, Taiwan, in 1983 and 1985, respectively, and the Ph.D. degree in electrical engineering from National Tsing Hua University, Taiwan, in 1993. From 2011 to 2019, he was the Chair and a Principle Investigator of the Smart Grid Focus Center, National Energy Project Phase I and II in Taiwan. He is currently a Chair Professor with the Department of Electrical Engineering, National Central University, Taiwan. His work has been widely cited. Several of his articles have helped to establish research areas, such as fuzzy neural network control of motor drives and motion control systems, and resonant converters for piezo-ceramic motor drives. His research interests include ac motor drives, power electronics, renewable energies, smart grids, and intelligent and nonlinear control theories. He is an IET Fellow. He received the Outstanding Research Awards from the National Science Council, Taiwan, in 2004, 2010, and 2013, and the Outstanding Professor of the Engineering Award, in 2016 from the Chinese Institute of Engineers, Taiwan. From 2012 to 2016, he was also the President of the Taiwan Smart Grid Industry Association. He was an Associate Editor of the IEEE Transactions on Fuzzy Systems. He is currently an Associate Editor of the IEEE Transactions on Power Electronics and the Executive Director of Taiwan Power Company.

KUANG-HSIUNG TAN received the B.S., M.S., and Ph.D. degrees from the Chung Cheng Institute of Technology (CCIT), National Defense University, Taiwan, China, in 2002, 2007, and 2013, respectively, all in electrical and electronic engineering.

He has been a Faculty Member with CCIT, where he is currently an Associate Professor with the Department of Electrical and Electronic Engineering. His teaching and research interests include power electronics, power quality, microgrid systems, and intelligent control.

WEN-CHOU LUO was born in Miaoli County, Taiwan, in 1994. He received the B.S. degree in electrical engineering from National United University, Miaoli, Taiwan, in 2017, and the M.S. degree in electrical engineering from National Central University, Chungli, Taiwan, in 2019. His research interests include active PV systems, intelligent control, and power electronics.

GUO-DENG XIAO was born in Changhua County, Taiwan, in 1996. He received the B.S. degree in electrical engineering from National Chung Cheng University, Chiayi, Taiwan, in 2018. He is currently pursuing the M.S. degree with National Central University, Chungli, Taiwan. His research interests include intelligent control and microgrid.

• • •